



# Non-Classical Hydrothermal Synthesis of Hexagonal Sodium Yttrium Fluoride Nanowires

Alexander B. Bard,<sup>†</sup> Xuezhe Zhou,<sup>‡</sup> Xiaojing Xia,<sup>¶</sup> Guomin Zhu,<sup>§,‡</sup> Matthew B. Lim,<sup>‡</sup> Seung Min Kim,<sup>||</sup> Matthew C. Johnson,<sup>⊥</sup> Justin M. Kollman,<sup>⊥</sup> Matthew A. Marcus,<sup>#</sup> Steven R. Spurgeon,<sup>©</sup> Daniel E. Perea,<sup>△</sup> Arun Devaraj,<sup>§</sup> Jaehun Chun,<sup>§</sup>  
James J. De Yoreo,<sup>§,‡,†</sup> and Peter J. Pauzauskie<sup>\*,‡,§,†</sup>

<sup>†</sup>*Department of Chemistry, University of Washington, Seattle, WA 98195, USA*

<sup>‡</sup>*Department of Materials Science and Engineering, University of Washington, Seattle, WA 98195, USA*

<sup>¶</sup>*Department of Molecular Engineering and Science, University of Washington, Seattle, WA 98195, USA*

<sup>§</sup>*Physical and Computational Sciences Directorate, Pacific Northwest National Laboratory, Richland, WA 99352, USA*

<sup>||</sup>*Institute of Advanced Composite Materials, Korea Institute of Science and Technology, Jeonbuk 565-905, Republic of Korea*

<sup>⊥</sup>*Department of Biochemistry, University of Washington, Seattle, WA 98195, USA*

<sup>#</sup>*Advanced Light Source, Lawrence Berkeley National Laboratory, Berkeley, CA 94720, USA*

<sup>©</sup>*Energy and Environment Directorate, Pacific Northwest National Laboratory, Richland, WA 99352, USA*

<sup>△</sup>*Environmental Molecular Sciences Laboratory, Earth and Biological Sciences Directorate, Pacific Northwest National Laboratory, Richland, WA 99352, USA*

E-mail: peterpz@uw.edu

## Abstract

Sodium yttrium fluoride ( $\text{NaYF}_4$ ) is an upconverting material with many potential uses in chemistry, materials science, and biology that can be synthesized hydrothermally in both cubic ( $\alpha$ ) and hexagonal ( $\beta$ ) crystallographic polymorphs. Understanding the mechanisms underlying the phase conversion between the cubic and hexagonal polymorphs is of great interest to help inform future efforts to synthesize atomically-precise quantum materials with well-defined sizes and morphologies. In this work, we use a combination of analytical and cryogenic transmission electron microscopy (TEM), scanning transmission electron microscopy (STEM), powder X-ray diffraction (XRD), in situ liquid cell TEM, atom probe tomography (APT), and extended x-ray absorption fine structure (EXAFS) measurements to show evidence suggesting that the hexagonal  $\text{NaYF}_4$  nanowires form through a non-classical crystal growth mechanism involving oriented attachment of grains of the cubic ( $\alpha$ ) phase. EXAFS spectroscopy also suggests that substitutional  $\text{Yb}^{3+}$  point defects within  $\text{NaYF}_4$  are distributed evenly throughout the crystal lattice without clustering, and also that they selectively substitute into one of the two possible trivalent yttrium sites in the unit cell.

## Introduction

Lanthanide-doped rare-earth fluoride crystals are a class of materials that have attracted great interest for decades due to their optical upconversion properties.<sup>1-4</sup> This has led to a wide range of applications in biomedicine,<sup>4-7</sup> solar energy,<sup>8-11</sup> anti-counterfeiting,<sup>12-14</sup> solid-state laser refrigeration,<sup>15-18</sup> and more recently, claims of enhanced night vision in living rodents.<sup>19</sup> Lanthanide-ions doped within fluoride crystals are also under active investigation for applications as long-lived optical quantum memories.<sup>20</sup> One important material is sodium yttrium fluoride ( $\text{NaYF}_4$ ), which has been studied not only for its optical and electronic properties,<sup>21-24</sup> but also for its morphological and crystallographic microstructure.<sup>4,25,26</sup> Traditionally,  $\text{NaYF}_4$  has been grown using high-temperature Czochralski methods,<sup>26-28</sup> but this

method has shown difficulties in obtaining single crystals of hexagonal particles due to large anisotropic thermal expansion coefficients.<sup>29</sup> Czochralski methods also make it difficult to study the mechanism by which these materials form at the atomic to nanometer level, indicating the need for alternative synthesis procedures.

In contrast to Czochralski single crystal growth, hydrothermal syntheses allow for safer, lower-cost, and more controlled growth of single-crystalline nanostructures.<sup>30-33</sup> This process, shown in Figure 1A, allows for an easily-controllable synthesis of either cubic ( $\alpha$ ) nanoparticles or hexagonal ( $\beta$ ) nanowires in an oleic acid microemulsion (Figure 1B), using only relatively non-toxic and inexpensive reagents, and temperatures easily reached by a standard laboratory oven. However, hydrothermal processes still take place at elevated temperatures and pressures inside a sealed autoclave, making it more challenging to probe the chemical and physical phenomena that govern the nucleation and growth of crystalline materials.<sup>34,35</sup> The thermodynamics of the phase conversion between the cubic and hexagonal polymorphs have been thoroughly studied,<sup>36,37</sup> indicating that the alpha phase nucleates first based on thermodynamics, considering both volumetric and surface contributions in free energy. Above a critical grain size, the hexagonal phase becomes more thermodynamically stable. However, classical thermodynamic calculations by their nature do not depend on complex kinetic and mechanistic phenomena that are encountered at particular synthesis conditions. For example, theoretical modeling of the solvation and diffusion of sodium ( $\text{Na}^+$ ) ions in water is still a subject under active investigation.<sup>38</sup> Furthermore, the solvation, chelation, and subsequent diffusion of ions in solution is complicated further by a ternary microemulsion system, varieties of which are frequently used in hydrothermal syntheses (Figure 1).<sup>39</sup> Moreover, if indeed the  $\alpha$  phase is more thermodynamically stable at small grain sizes, then the cubic phase is also likely to appear first during crystallization, raising fundamental questions about how the formation of the hexagonal  $\beta$ - $\text{NaYF}_4$  nanowires relates to initial synthesis of the cubic phase. In this manuscript we propose a non-classical mechanism for the  $\alpha$  to  $\beta$  phase transition based on data collected by quenching the synthesis at various time

points. We use techniques such as cryogenic transmission electron microscopy (cryo-TEM), powder X-ray diffraction (XRD), extended X-ray absorption fine structure (EXAFS), and atom probe tomography (APT) to study the properties of the materials, and carefully examine the final products to elucidate the mechanism by which they form at a microstructural level.

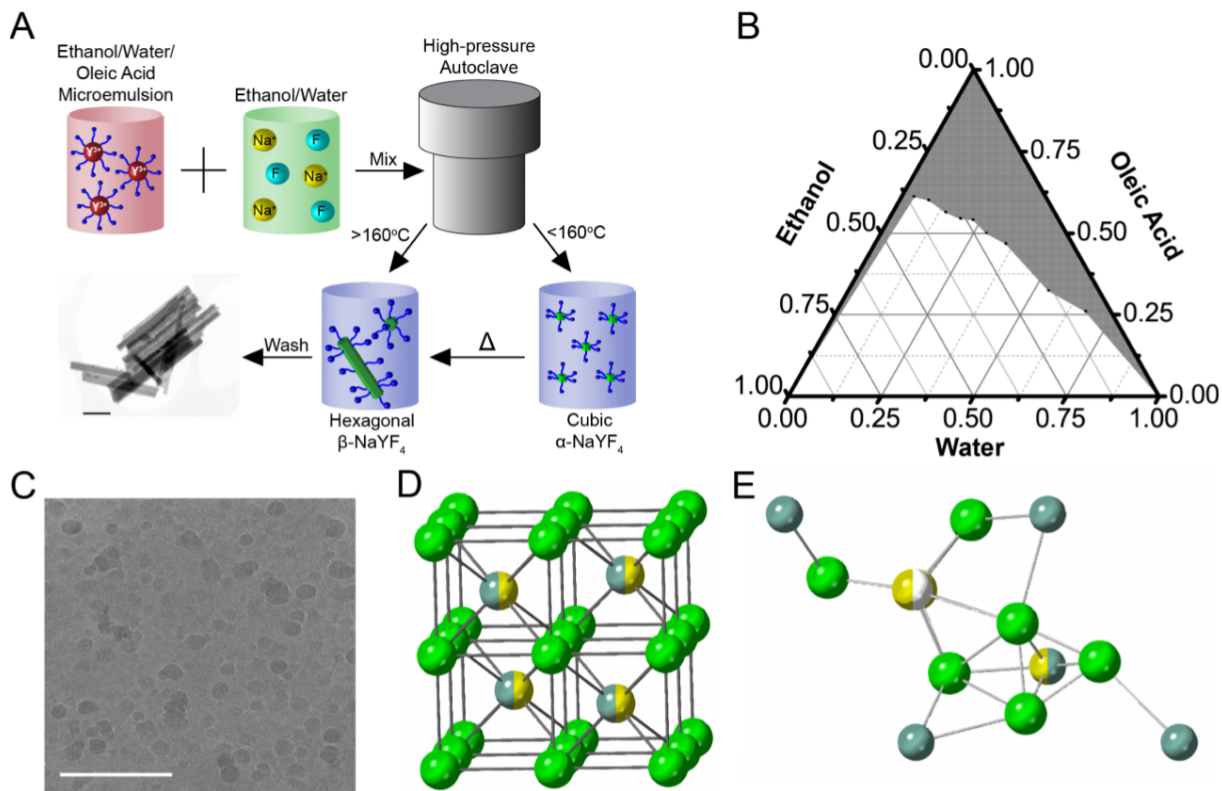


Figure 1: (A) Hydrothermal synthesis of  $\text{NaYF}_4$  (scale bar on STEM image = 500 nm) and (B) ternary phase diagram for water/ethanol/oleic acid microemulsion. Shaded region is microemulsion and unshaded region is heterogeneous mixture. (C) Cryo-TEM of early-stage mixture showing microemulsion at 77 K. Scale bar = 200 nm. (D) Cubic and (E) Hexagonal crystal structures for  $\text{NaYF}_4$ , yellow = Na, blue = Y, Yb, green = F, white = vacancy. Half-shaded atoms indicate split occupancy.

One difficulty in characterizing this phase conversion mechanism is that there are discrepancies in the literature regarding the exact crystal structure of the hexagonal phase.<sup>40–46</sup> While it is clear that the crystal structure of  $\beta\text{-NaYF}_4$  is hexagonal in nature, the occupancy of the cation sites and the level of delocalization is a matter of discussion. For example, Grzechnik showed in 2002 that these factors change as a function of pressure,<sup>40</sup> but molecu-

lar dynamics calculations by Szefczyk in 2014 showed that it is theoretically possible for any of the three most widely reported crystal structures to exist at atmospheric conditions.<sup>41</sup> It should be further noted that, to our knowledge, all single crystal XRD studies of  $\beta$ -NaYF<sub>4</sub> have been done on Czochralski-grown materials, which cannot be assumed to undergo the same phase conversion mechanism as hydrothermal  $\beta$ -NaYF<sub>4</sub>. For this reason, the crystal structure between the two may not necessarily be identical.

The cubic crystal structure is well-characterized as a solid solution of tetrahedrally-arranged sodium and rare earth cations with an opposing tetrahedron of vacancies in a cubic lattice of fluoride ions, analogous to the well-known fluorite crystal structure (Figure 1D).<sup>44,47</sup> Notably, the sodium and rare earth ions are arranged randomly on the cation sites, meaning that a phase transition to one of the known  $\beta$ -NaYF<sub>4</sub> structures would likely necessitate the ordering of certain cations. This ordering is straightforward to consider in a Czochralski process that passes through a liquid/solid-phase or a classical hydrothermal process. However, it is more difficult to contemplate in a system that undergoes non-classical crystal growth such as oriented attachment (OA).<sup>48</sup> Nonetheless, in light of recent results on a number of systems that similarly produce nanowires of a bulk phase starting from primary particles of a transient nanoscopic phase via OA,<sup>49,50</sup> this mechanism of  $\beta$ -NaYF<sub>4</sub> nanorod formation must be considered.

During OA, crystal growth mostly proceeds by assembly of primary particles that typically attach on lattice-matched faces, for example by crystallographic alignment on a twin plane,<sup>51-56</sup> to form the final bulk crystal. This mechanism stands in contrast to classical growth processes that proceed through ion-by-ion addition to atomic steps on the crystal surface.<sup>53</sup> While the primary particles are typically of the same phase as the secondary particles, oriented attachment can also occur in systems where primary particles of a different phase either transform before attaching,<sup>50</sup> attach on faces of the secondary particle that nonetheless produce a lattice match,<sup>49</sup> or attach to form a disordered aggregate that evolves to a single crystal over time.<sup>57,58</sup> Which of these mechanisms would be the most probable

for hexagonal NaYF<sub>4</sub> formation from cubic NaYF<sub>4</sub> is not clear *a priori*, but a fundamental understanding of the dominant mechanism, whether it be classical or via one of the previously mentioned OA pathways, is important for the optimization of growth and performance of these materials.

In this work, we present a multifaceted approach to understand the fundamental growth mechanism of  $\beta$ -NaYF<sub>4</sub> nanowires under hydrothermal conditions. Firstly, we present a "time series" approach in which we study the properties of NaYF<sub>4</sub> particles synthesized in reactions that were quenched before the  $\beta$ -NaYF<sub>4</sub> could fully form, using TEM and XRD to study the evolution of their physical and chemical properties. We then transition to a "post-growth" approach in which we study the properties of fully-formed  $\beta$ -NaYF<sub>4</sub> and  $\alpha$ -NaYF<sub>4</sub> particles using TEM, Energy Dispersive X-ray Spectroscopy (EDS), Electron Energy Loss Spectroscopy (EELS), atom probe tomography (APT), and EXAFS to examine the particles for chemical insights into how they form.

## Experimental

### Hydrothermal Synthesis of NaYF<sub>4</sub>

2 mL of a 2.875 M aqueous NaOH solution were added to 8 mL of 100% ethanol. 3 mL of oleic acid were then added to the mixture while stirring. 1 mL of a 1 M aqueous RECl<sub>3</sub> stock solution (RE = 90%Y, 10%Yb or 100% Y) was then added to the mixture (Solution A) and it was stirred for 30 minutes. Meanwhile, 4 mmol of NaF were dispersed in 3 mL of water and 3 mL of ethanol (Solution B). Solution B was added to Solution A dropwise while stirring. After 30 minutes of stirring, the mixture was transferred into a PTFE-lined stainless steel autoclave (Parr 4747, 25 mL) and sealed. The autoclave was placed in a 200°C oven for a specified amount of time, T<sub>s</sub>, and then allowed to return to room temperature. The product was washed and centrifuged with both ethanol and water. T<sub>s</sub> is 24 hours for the full synthesis, and it was varied from 30 minutes to 8 hours for the time series.  $\alpha$ -NaYF<sub>4</sub>

particles were synthesized by the same procedure, except the synthesis was heated to only 100°C, keeping the same  $T_s$  of 24 hours.

## TEM Measurements

TEM images were taken on an FEI G<sup>2</sup> TECNAI F20 S/TEM at 200 kV with a Gatan Ultra-scan CCD camera. For in situ measurements, a three-hour NaYF<sub>4</sub> sample was dispersed in water and dropcast into a Hummingbird static liquid cell TEM holder and imaged through silicon nitride windows. Tomographic reconstructions were built using publicly available Matlab code.<sup>59</sup> STEM samples were prepared by dropcasting particles sonicated in a dilute suspension onto a lacey carbon grid. High-angle annular dark field (STEM-HAADF) images were collected on a JEOL GrandARM-300F microscope operating at 300 kV, with a convergence semi-angle of 29.7 mrad and an inner collection angle of 75 mrad. Energy-dispersive X-ray spectroscopy (STEM-EDS) maps were collected using a dual JEOL Centurio detector setup ( $\sim 1.6$  sr solid angle), with a 1 Å probe size, roughly 237 pA probe current, 10  $\mu$ s px<sup>-1</sup> dwell time, and a roughly 3.5 min total acquisition time. Electron energy loss spectroscopy (STEM-EELS) maps were collected using the same probe settings and a spectrometer acceptance angle of roughly 113 mrad, with a 1 eV ch<sup>-1</sup> energy dispersion, 10 ms px<sup>-1</sup> dwell time, and 6 min 18 s total acquisition time. The spectrometer was fully binned in the non-dispersive axis to improve signal-to-noise. No plural scattering correction was performed and no principal component analysis (PCA) or other denoising was applied.

## Cryo-TEM Measurements

Small volumes (3.5  $\mu$ L) were taken directly from a stirred vessel containing the NaYF<sub>4</sub> reaction mixture at room temperature at several timepoints. These were applied to glow-discharged C-flat holey carbon EM grids (Protochips), blotted, and plunge-frozen in liquid ethane with an FEI Vitrobot plunge-freezing device. Grids were stored under liquid nitrogen until imaging, which was done using an FEI TECNAI G<sup>2</sup> Spirit operating at 120 kV and

liquid nitrogen temperature, and a Gatan Ultrascan 2000 CCD. Automated data collection was accomplished via the Legimon software package.<sup>60</sup>

## EXAFS Measurements

Samples for EXAFS were prepared by dropcasting a suspension of  $\beta$ -NaYF<sub>4</sub> in water onto an X-ray transparent polyimide (Kapton) tape substrate. The sample was placed in the LBNL ALS Beamline 10.3.2 under a helium environment. Hard X-rays were focused on the sample around the Yb L3-edge, from 8.8-9.9 keV. Two scans were taken in QXAS (continuous-scan) mode, with count time/point increasing roughly linearly in the post-edge region from 4 to 11 seconds. Data were taken in fluorescence and transmission mode simultaneously. The two fluorescence scans were pre-edge subtracted, post-edge normalized, corrected for overabsorption, then averaged.

## EXAFS Analysis

Our model was fit based on the  $P\bar{6}$  structure of  $\beta$ -NaYF<sub>4</sub> as reported by Grzechcnik.<sup>40</sup> This model has a unit cell stoichiometry of Na<sub>1.5</sub>Y<sub>1.5</sub>F<sub>6</sub> with two Y sites, one of which (Y2) is half-occupied and shared with a half-occupied Na site (Na1) at the same position. There is another Na site (Na2), which is half-occupied. We made the assumption that all Yb dopants would substitute in a Y site. Because split occupancy crystal structures are incompatible with the use of FEFF<sup>61</sup> and Artemis,<sup>62</sup> we modified the unit cell such that it contained two of the original  $P\bar{6}$  unit cells with full occupancy of Y and Na, respectively. For further details on this modification, see the supporting information. Shell-by-shell fitting was performed using Artemis running FEFF6l. These fits were done in  $q$ -space with a distance range of 1-4.5 Å, a  $k$ -weight exponent of 3, and a  $q$  range of 2-14 Å<sup>-1</sup>.

## DLS Measurements

Dynamic light scattering (DLS) measurements were taken on a Malvern ZEN3600 Zetasizer™ Nano-ZS with a 633 nm red laser. NaYF<sub>4</sub> samples were centrifuged and rinsed 3 times with Millipore water, and resuspended in Millipore water before final DLS measurements. Particle size measurements were taken in 1 cm polystyrene cuvettes, and zeta potential measurements were taken in Malvern disposable folded capillary cells.

## FTIR Measurements

Fourier-Transform Infrared (FTIR) spectra were taken on a Bruker VERTEX 70v FTIR Spectrometer in attenuated total reflectance (ATR) mode. Powdered NaYF<sub>4</sub> samples were placed on the diamond ATR crystal and 16 scans were averaged. The spectral resolution of the instrument is 2 cm<sup>-1</sup>.

## XRD Measurements

Powder X-Ray Diffraction (XRD) samples were prepared by dropcasting a concentrated slurry of sample onto <100> silicon wafers. Spectra were taken on a Bruker D8 Discover Microfocus diffractometer with a Dectris Pilatus3 R 100K-A 2D detector and a Cu K $\alpha$  X-ray source with a 0.5 mm collimator. A Coupled  $2\theta/\theta$  scan was performed from 16° to 93° with a 5.5° increment to create overlap, with a scan time of 30 seconds per  $\theta$ . During the scans, the sample was oscillated in the x, y, and  $\phi$  directions to remove the effects of texture and improve statistics. An air scatter screen was used to reduce background. Scans were integrated, indexed, processed, and analyzed using Bruker Diffrac.Eva software.

## APT Measurements

Atom probe tomography (APT) samples were prepared from  $\beta$ -NaYF<sub>4</sub> nanorods using a FEI Helios Nanolab DualBeam scanning electron microscope/focused ion beam. APT was per-

formed using a Cameca LEAP 4000X-HR housed at the Environmental Molecular Sciences Laboratory at the Pacific Northwest National Laboratory. The detected ion count rate was set to 300 ions per second using a 355 nm UV laser pulsed at 100 kHz. The specimen stage temperature was 44K. The data were processed using IVAS software version 3.8.

## Results and discussion

In order to elucidate details about the crystal structure of the hexagonal  $\beta$ -NaYF<sub>4</sub>, we used extended X-ray absorption fine structure (EXAFS) spectroscopy to study the ytterbium centers in doped  $\beta$ -NaYF<sub>4</sub> (Figure 2). EXAFS spectra were fit to a known  $P\bar{6}$  crystal structure for  $\beta$ -NaYF<sub>4</sub>,<sup>40</sup> modified for compatibility with FEFF, as discussed previously. These data were then processed and fit with a variety of models to determine the spacing and occupancy of the ytterbium atoms. The  $P\bar{6}$  unit cell for  $\beta$ -NaYF<sub>4</sub> has a stoichiometry of Na<sub>1.5</sub>Y<sub>1.5</sub>F<sub>6</sub>, with one Y<sup>3+</sup> ion (Y1) residing on the corner and the remaining half-ion (Y2) in an internal split-occupancy site with sodium (Figure 1E). Ytterbium replaces these yttrium ions in the doped structure, so EXAFS models were fit with Yb<sup>3+</sup> in both of those sites. Surprisingly, the fit only improved in quality when the only substitution was in the Y1 site, suggesting that Yb does not dope into the split-occupancy Y2 site. Otherwise, the EXAFS data fit well with our substituted  $P\bar{6}$  model, except with most distances shorter, which can be explained by the smaller ionic radius of Yb<sup>3+</sup> as compared to Y<sup>3+</sup>. Further insights into the synthesis mechanism and the resulting crystal structure can be gathered by considering how lanthanide dopants incorporate into the crystal matrix.<sup>63,64</sup> This is useful not only for our own mechanistic studies, but also for myriad other studies involving the upconversion properties of lanthanide-doped NaYF<sub>4</sub>.<sup>15,65,66</sup> Specifically, the dopant can be uniformly distributed, or it might undergo some sort of clustering, which could result in fluorescence quenching.<sup>67-69</sup> To determine whether the Yb dopant clusters, a model was fit with some of the nearest Y1 sites replaced with Yb<sup>3+</sup>. This decreased the quality of the fit,

suggesting that the nearest rare earth neighbors to ytterbium in this structure are yttrium ions, and therefore that the ytterbium dopant does not cluster.

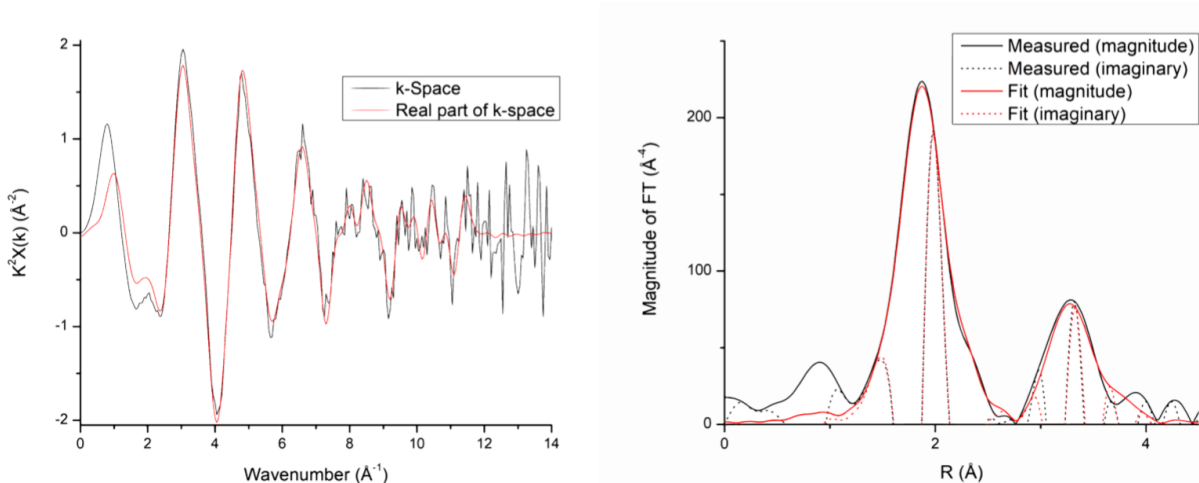


Figure 2: EXAFS analysis of  $\beta$ -NaYF<sub>4</sub>:10%Yb nanowires. (A) EXAFS data in k space. (B) Fourier transformed Yb spacing data and calculated best fit.

By varying the time of synthesis,  $T_s$ , from 30 minutes to eight hours, we show using TEM and XRD (Figure 3) that the cubic  $\alpha$  phase nucleates within minutes, while the hexagonal  $\beta$  phase first nucleates around one hour. After four hours in the oven, the  $\beta$  phase is the only phase detectable by XRD (Figure 3D), though it should be noted that a small amount of  $\alpha$ -NaYF<sub>4</sub> still remains after even 24 hours. A Scherrer analysis of these XRD spectra (Figure 3E) shows that the  $\beta$ -NaYF<sub>4</sub> nucleates with a diameter much larger than that which the  $\alpha$ -NaYF<sub>4</sub> ever achieves. It should be emphasized that the maximum size measurable with a Scherrer analysis is generally on the order of 100 nanometers, depending on the precision of the spectrometer and the number of reflections measured,<sup>70,71</sup> and as such, we cannot use this method to determine that the  $\beta$ -particles nucleate at any specific size, but rather that they nucleate much larger than the  $\alpha$ -NaYF<sub>4</sub> particles, and that the  $\alpha$ -NaYF<sub>4</sub> particles continue to grow even after the  $\beta$ -NaYF<sub>4</sub> particles have already formed. This is consistent with the hypothesis that the hexagonal ( $\beta$ ) phase nanowires are not nucleating by a classical crystal growth mechanism, in which they would grow steadily as the feedstock dissolves.<sup>72-74</sup> In fact, the Scherrer analysis illustrates that the  $\alpha$ -NaYF<sub>4</sub> particles continue to grow with time rather

than dissolve, which supports the argument that the phase conversion mechanism is non-classical. This is additionally supported by experiments in which we nucleated  $\alpha$ -NaYF<sub>4</sub> with and without lanthanide dopant ions, in which the doped sample had 20% Yb and 2% Er, and then we mixed the doped and undoped samples and heated in order to form a partially-doped  $\beta$ -NaYF<sub>4</sub>. A STEM-EDS analysis of these particles (Figure S1) shows that the ytterbium concentration is not homogeneous across the rods, suggesting that they are not forming from a homogeneous solution. These observations are corroborated by TEM images (Figure 3A-C) which show  $\beta$  particles first appearing orders of magnitude larger than the  $\alpha$  particles. TEM images of particles at short synthesis times are also consistent with a non-classical growth mechanism, as shown in Figure 4B, after a 160 minute synthesis, as compared to the 24 hour synthesis in Figures 4C-E. Here we directly examined the crystal lattice for moiré fringes, which suggest minor deviations from perfect crystallographic alignment,<sup>75</sup> and examined the Fast Fourier Transform (FFT) of the crystal matrix, which is related to a diffraction pattern and shows the degree of single crystallinity through the spreading (or lack thereof) of the spots.<sup>76</sup> The moiré fringes in Figure 4B, as well as direct observations of the lattice fringes and the FFT, indicate that that particle is not perfectly single crystalline, unlike the much more uniform lattice fringes in Figure 4D, after a longer synthesis. This is consistent with the hypothesis that the  $\beta$ -NaYF<sub>4</sub> is formed by smaller crystallites that undergo an oriented attachment process to form the larger crystal.<sup>77</sup>

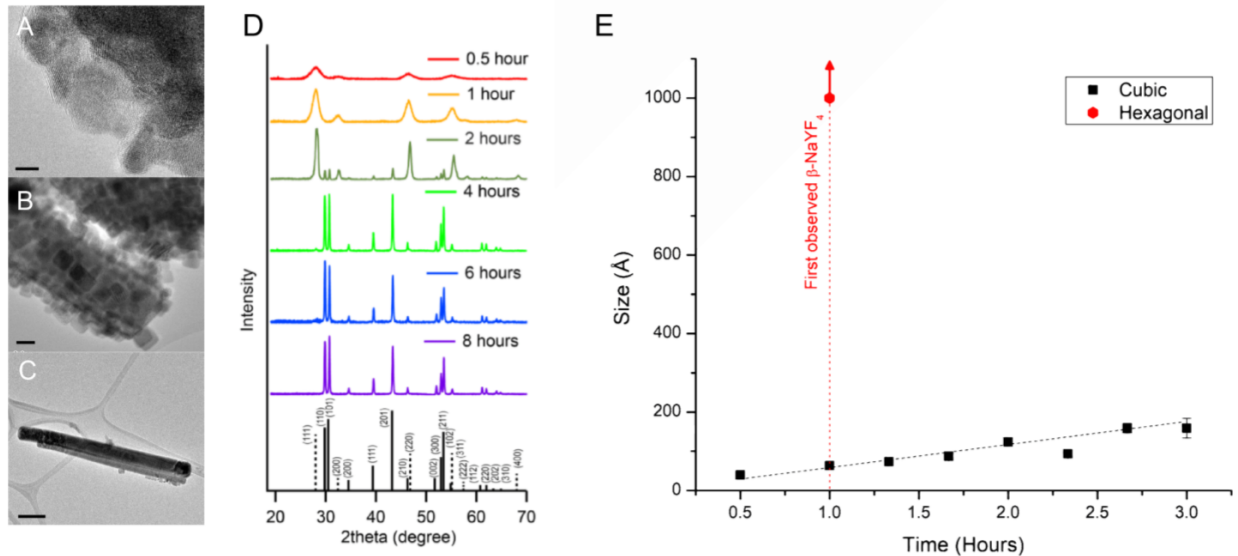


Figure 3: (A-C) TEM images of the progression of NaYF<sub>4</sub> growth at (a) one hour, (b) two hours, and (c) 24 hours. Scale bar A = 5 nm, B = 50 nm, C = 200 nm. (D) Powder XRD study of NaYF<sub>4</sub> growth at selected time points. Dashed black lines represent the theoretical α-NaYF<sub>4</sub> peaks and solid black lines represent the theoretical β-NaYF<sub>4</sub> peaks. (E) Scherrer analysis of XRD spectra. β-NaYF<sub>4</sub> is first observed at the one hour time point at a size that is already too large to measure with a Scherrer analysis.

Even after a 24-hour synthesis, small ( $\sim 30$  nm), morphologically cubic particles remain on the surface of the nanowires, as can be seen in the TEM tomographic reconstruction in Figure 4A and in the TEM image in Figure 4B, though it should be noted that their overall mass fraction becomes too low for them to be observed with XRD after about three hours. By measuring the d-spacing from the HRTEM image (Figure 4E) as  $2.71 \text{ \AA}$  and comparing the projection and FFT to simulated crystal axes of possible species in the synthesis vessel, the image in Figure 4E was indexed to the [100] projection of α-NaYF<sub>4</sub> (Figure S2). This demonstrates that α particles can not only survive the high temperature synthesis conditions but that they continue to grow and form morphological structures even in the immediate presence of β particles. Additionally, an amorphous coating appears to be present on the end cap of the β-NaYF<sub>4</sub> rod and on all surfaces of the α-NaYF<sub>4</sub> cube (Figure 4B). EDS mapping data is consistent with the presence of oleate, as discussed further below. Density functional theory calculations by Sui et al.<sup>78</sup> suggest that oleate can influence the growth of

NaYF<sub>4</sub> in several ways, which leads us to hypothesize that the presence of sodium oleate on the end caps influences the morphology of the final particles.

The presence of sodium oleate in those end caps is suggested by EELS and EDS maps of the sodium content of the nanowires (Figure 5). The EDS map in Figure 5F indicates an enrichment in sodium on the caps, and the EELS map in Figure 5B shows clearly that the sodium is aggregating on the caps rather than the sides of the wires, as well as uniformly around  $\alpha$ -NaYF<sub>4</sub> particles. The apparent lack of sodium within the nanowires in the EELS map can be attributed to multiple scattering as a result of the thickness of the particles.<sup>79</sup> The superposition of the sodium and the fluorine EELS maps (Figure 5D) shows that the sodium is present in regions of amorphous material outside of the nanowire, and preferentially on the tips, rather than it accumulating within the structure. This behavior indicates that there is sodium in that amorphous material, which is consistent with our hypothesis that that material is sodium oleate. This finding is further supported by a mass spectrum of the surface, measured with atom probe tomography (APT, Figure S3), which shows several organic groups and sodium, but no yttrium, indicating that we are only measuring the material on the end cap. The fact that we observe this enhancement of oleate on a particular face leads us to hypothesize that it is relevant to the growth mechanics of the crystal, and the specific nature of this influence is the subject of potential future work.

Dynamic light scattering (DLS) measurements (Table S4) show a significant change in zeta potential during the phase conversion. The  $\alpha$ -phase is observed to have a highly negative zeta potential in water (-70mV), while the final  $\beta$ -phase has a positive zeta potential in water (+20mV). Although the zeta potentials reported here likely differ from those within the hydrothermal microemulsion, along with an intrinsic complexity due to the random orientation of non-spherical particles,<sup>80</sup> it is possible that the kinetics of oriented assembly of the  $\alpha$ -phase could be significantly altered as the magnitude of the zeta potential becomes less negative during the transition to the  $\beta$ -phase. The different zeta potentials may also explain the TEM observation of cubic  $\alpha$ -phase grains attached to the surface of  $\beta$ -phase

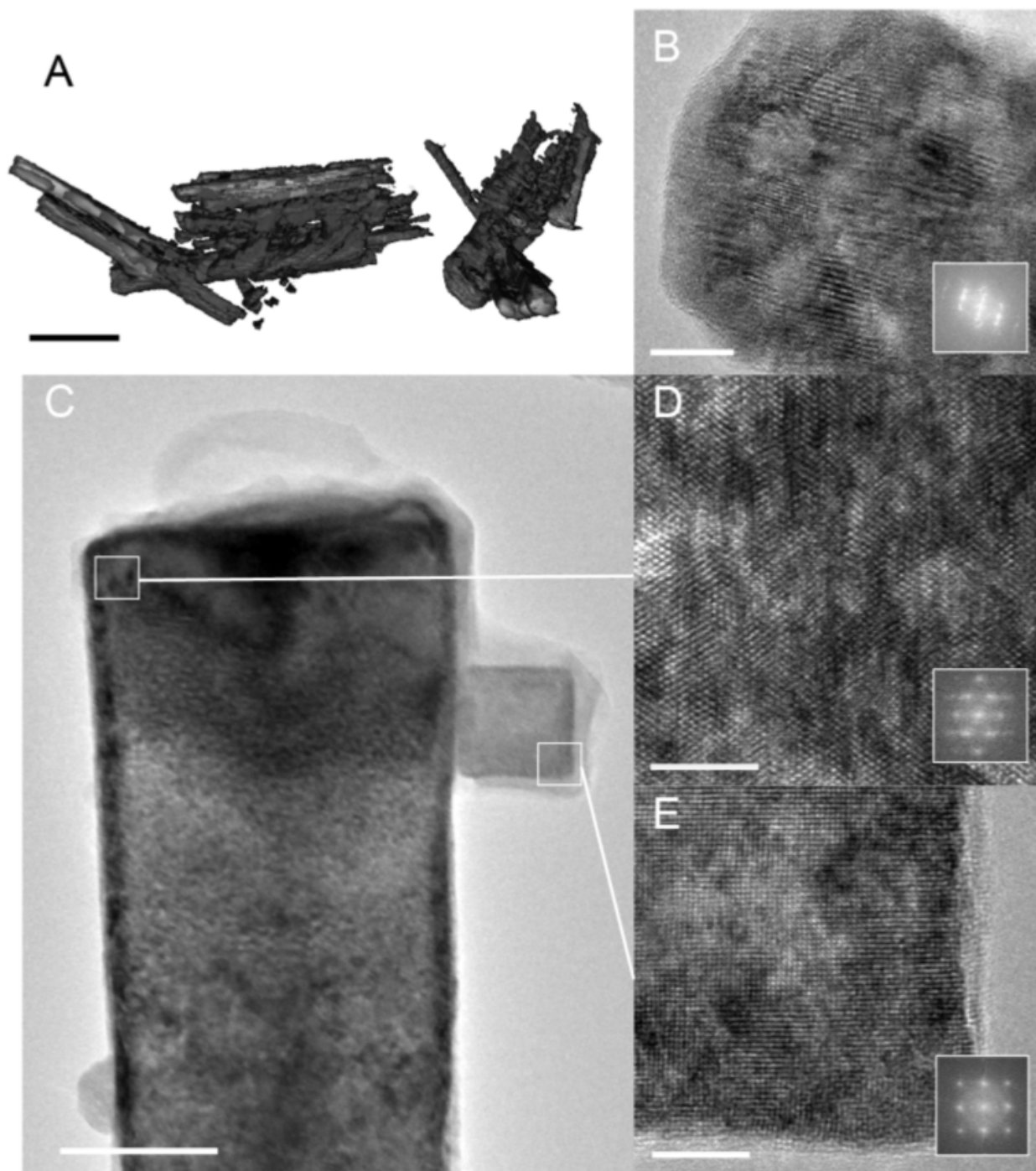


Figure 4: (A) Tomographic reconstructions of clustered  $\beta$ -NaYF<sub>4</sub> particles with  $\alpha$ -NaYF<sub>4</sub> particles on the surface. Scale = 500 nm. (B) TEM image and FFT of a  $\beta$ -NaYF<sub>4</sub> particle after a 160 minute synthesis, noting the slight crystallographic mismatch evident in the lattice. Scale = 10 nm. (C) TEM image of a  $\beta$ -NaYF<sub>4</sub> particle (left) with an  $\alpha$ -NaYF<sub>4</sub> particle on the surface (right). Scale = 50 nm. (D,E) HRTEM images of  $\beta$ - and  $\alpha$ -NaYF<sub>4</sub> particles, respectively. Scale = 5 nm.

NWs.

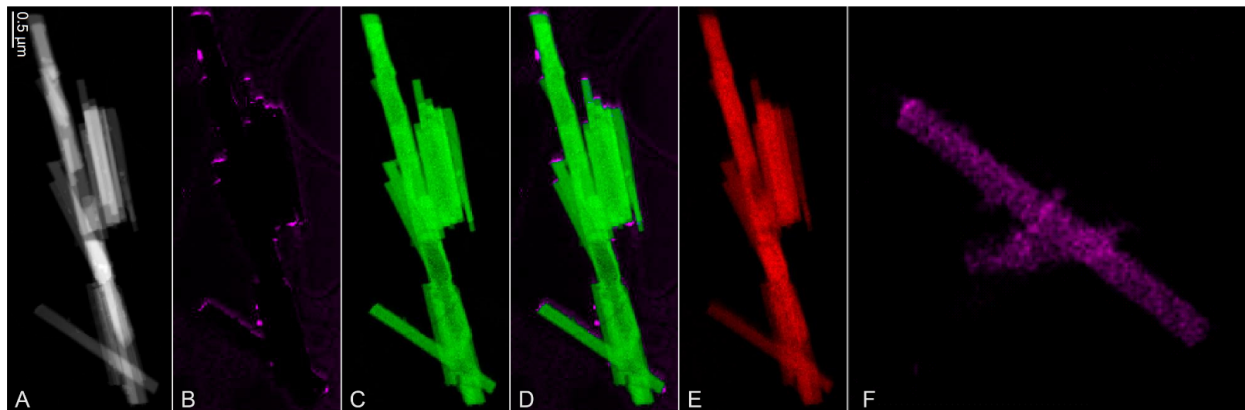


Figure 5: (A) STEM HAADF image of  $\text{NaYF}_4$  cluster (scale = 500 nm). (B-E) EELS maps of (B) Na-K edge, (C) F-K edge, (D) Na + F, (E) Y-L edge. (F) EDS map of Na-K edge (on a different cluster of  $\text{NaYF}_4$  at the same magnification).

## Conclusions

In this work, we show several data sets consistent with the hypothesis that hexagonal  $\text{NaYF}_4$  nanowires synthesized by a hydrothermal method do not form through classical crystal growth mechanisms but rather through a non-classical mechanism involving oriented attachment. The proposed oriented attachment component of this mechanism suggests that this hydrothermal synthesis could be used to build nanoparticles from multiple components, which could be employed in nanoscale devices with novel optoelectronic properties. EXAFS measurements suggest that the  $\text{Yb}^{3+}$  ions in doped  $\text{NaYF}_4$  are evenly distributed across the crystal lattice rather than clustering, and that the Yb doping is site-specific in the  $\beta\text{-NaYF}_4$  structure. This finding motivates future work using low-temperature spectroscopy to further investigate the site-specific nature of the doping.<sup>81</sup> Furthermore, a thorough understanding of the synthesis mechanism based on particle interactions can inform future experiments meant to direct the morphology of  $\beta\text{-NaYF}_4$  particles, and could even help to design a predictive model to control the morphology and size of  $\text{NaYF}_4$  materials.

## Acknowledgement

Mechanistic studies based on XRD, SEM, FTIR, DLS, *in situ* TEM, STEM, and subsequent analyses and interpretations were performed with support from the US Department of Energy, Office of Science, Basic Energy Sciences, Division of Materials Sciences and Engineering, under Award KC020105-FWP12152 as well as with support from the Northwest Institute for Materials Physics, Chemistry, and Technology (NW IMPACT) which is a joint research collaboration of the U.S. Department of Energy's Pacific Northwest National Laboratory and the University of Washington. PNNL is operated by Battelle for the Department of Energy under contract no. DE-AC05-76RLO1830. EXAFS measurements were performed at the Advanced Light Source. The operations of the Advanced Light Source are supported by the Director, Office of Science, Office of Basic Energy Sciences, US Department of Energy under Contract No. DE-AC02-05CH11231. TEM and XRD measurements were conducted at the Molecular Analysis Facility, a National Nanotechnology Coordinated Infrastructure site at the University of Washington which is supported in part by the National Science Foundation (grant ECC-1542101), the University of Washington, the Nanoengineering & Systems Institute. STEM imaging was performed in the Radiological Microscopy Suite (RMS), located in the Radiochemical Processing Laboratory (RPL) at PNNL. APT measurements were performed at PNNL using EMSL (grid.436923.9), a DOE Office of Science User Facility sponsored by the Office of Biological and Environmental Research. The authors acknowledge S. Manandhar for assistance in acquiring APT data.

## Supporting Information Available

The following files are available free of charge.

- HCHA\_SupportingInformation.pdf: Supporting Information

## References

- (1) Krämer, K. W.; Biner, D.; Frei, G.; Güdel, H. U.; Hehlen, M. P.; Lüthi, S. R. Hexagonal Sodium Yttrium Fluoride Based Green and Blue Emitting Upconversion Phosphors. *Chemistry of Materials* **2004**, *16*, 1244–1251.
- (2) Zhang, F.; Wan, Y.; Yu, T.; Zhang, F.; Shi, Y.; Xie, S.; Li, Y.; Xu, L.; Tu, B.; Zhao, D. Uniform Nanostructured Arrays of Sodium Rare-Earth Fluorides for Highly Efficient Multicolor Upconversion Luminescence. *Angewandte Chemie International Edition* **2007**, *46*, 7976–7979.
- (3) Kim, W. J.; Nyk, M.; Prasad, P. N. Color-Coded Multilayer Photopatterned Microstructures Using Lanthanide(III) Ion Co-Doped NaYF<sub>4</sub> Nanoparticles With Upconversion Luminescence for Possible Applications in Security. *Nanotechnology* **2009**, *20*, 185301.
- (4) Wang, S.; Feng, J.; Song, S.; Zhang, H. Rare Earth Fluorides Upconversion Nanophosphors: From Synthesis to Applications in Bioimaging. *CrystEngComm* **2013**, 7142–7151.
- (5) Guo, H.; Qian, H.; Idris, N. M.; Zhang, Y. Singlet Oxygen-Induced Apoptosis of Cancer Cells Using Upconversion Fluorescent Nanoparticles as a Carrier of Photosensitizer. *Nanomedicine: Nanotechnology, Biology and Medicine* **2010**, *6*, 486–495.
- (6) Sojka, B.; Kuricova, M.; Liskova, A.; Bartusova, M.; Banski, M.; Misiewicz, J.; Dusinska, M.; Horvathova, M.; Jahnova, E.; Ilavska, S.; Szabova, M.; Rollerova, E.; Podhorodecki, A.; Tulinska, J. Hydrophobic Sodium Fluoride-Based Nanocrystals Doped with Lanthanide Ions: Assessment of *In Vitro* Toxicity to Human Blood Lymphocytes and Phagocytes. *Journal of Applied Toxicology* **2014**, *34*, 1220–1225.
- (7) Chatterjee, D. K.; Yong, Z. Upconverting Nanoparticles as Nanotransducers for Photodynamic Therapy in Cancer Cells. *Nanomedicine* **2008**, *3*, 73–82.

- (8) de Wild, J.; Meijerink, A.; Rath, J. K.; van Sark, W. G. J. H. M.; Schropp, R. E. I. Environmental Science Upconverter Solar Cells: Materials and Applications. *Energy and Environmental Science* **2011**, 4835–4848.
- (9) Shalav, A.; Richards, B. S.; Trupke, T.; Krämer, K. W.; Güdel, H. U. Application of NaYF<sub>4</sub>:Er<sup>3+</sup> Up-Converting Phosphors for Enhanced Near-Infrared Silicon Solar Cell Response. *Applied Physics Letters* **2005**, 86, 013505.
- (10) Arnaoutakis, G. E.; Marques-Hueso, J.; Ivaturi, A.; Fischer, S.; Goldschmidt, J. C.; Krämer, K. W.; Richards, B. S. Enhanced Energy Conversion of Up-Conversion Solar Cells by the Integration of Compound Parabolic Concentrating Optics. *Solar Energy Materials and Solar Cells* **2015**, 140, 217–223.
- (11) Zhang, X. D.; Jin, X.; Wang, D. F.; Xiong, S. Z.; Geng, X. H.; Zhao, Y. Synthesis of NaYF<sub>4</sub>:Yb,Er Nanocrystals and Its Application in Silicon Thin Film Solar Cells. *physica status solidi (c)* **2010**, 7, 1128–1131.
- (12) Zhang, Y.; Zhang, L.; Deng, R.; Tian, J.; Zong, Y.; Jin, D.; Liu, X. Multicolor Barcoding in a Single Upconversion Crystal. *Journal of the American Chemical Society* **2014**, 136, 4893–4896.
- (13) Dejneka, M. J.; Streltsov, A.; Pal, S.; Frutos, A. G.; Powell, C. L.; Yost, K.; Yuen, P. K.; Muller, U.; Lahiri, J. Rare Earth-Doped Glass Microbarcodes. *Proceedings of the National Academy of Sciences* **2003**, 100, 389–393.
- (14) Zhang, F.; Haushalter, R. C.; Haushalter, R. W.; Shi, Y.; Zhang, Y.; Ding, K.; Zhao, D.; Stucky, G. D. Rare-Earth Upconverting Nanobarcode for Multiplexed Biological Detection. *Small* **2011**, 7, 1972–1976.
- (15) Zhou, X.; Smith, B. E.; Roder, P. B.; Pauzauskie, P. J. Laser Refrigeration of Ytterbium-Doped Sodium-Yttrium-Fluoride Nanowires. *Advanced Materials* **2016**, 28, 8658–8662.

- (16) Roder, P. B.; Smith, B. E.; Zhou, X.; Crane, M. J.; Pauzauskie, P. J. Laser Refrigeration of Hydrothermal Nanocrystals in Physiological Media. *Proceedings of the National Academy of Sciences* **2015**, *112*, 15024–15029.
- (17) Dong, G.-Z.; Zhang, X.-L.; Li, L. Energy Transfer Enhanced Laser Cooling in  $\text{Ho}^{3+}$  and  $\text{Tm}^{3+}$ -Codoped Lithium Yttrium Fluoride. *Journal of the Optical Society of America B* **2013**, *30*, 939.
- (18) Zhong, B.; Luo, H.; Chen, L.; Shi, Y.; Yin, J. Laser Cooling Performance of  $\text{Yb}^{3+}$ -Doped  $\text{LuLiF}_4$  Crystal. *Proceedings of SPIE*. 2016; p 976506.
- (19) Ma, Y.; Bao, J.; Zhang, Y.; Li, Z.; Zhou, X.; Wan, C.; Huang, L.; Zhao, Y.; Han, G.; Xue, T. Mammalian Near-Infrared Image Vision Through Injectable and Self-Powered Retinal Nanoantennae. *Cell* **2019**, *177*.
- (20) Minnegaliev, M.; Dyakonov, I.; Gerasimov, K.; Kalinkin, A.; Kulik, S.; Moiseev, S.; Saygin, M. Y.; Urmancheev, R. Observation and Investigation of Narrow Optical Transitions of  $^{167}\text{Er}^{3+}$  Ions in Femtosecond Laser Printed Waveguides in  $^7\text{LiYF}_4$  Crystal. *Laser Physics Letters* **2018**, *15*, 045207.
- (21) Ivanova, S. E.; Tkachuk, A. M.; Mirzaeva, A.; Pellé, F. Spectroscopic Study of Thulium-Activated Double Sodium Yttrium Fluoride  $\text{Na}_{0.4}\text{Y}_{0.6}\text{F}_{2.2}:\text{Tm}^{3+}$  Crystals: I. Intensity of Spectra and Luminescence Kinetics. *Optics and Spectroscopy* **2008**, *105*, 228–241.
- (22) Tkachuk, A. M.; Ivanova, S. É.; Joubert, M. F.; Guyot, Y. Spectroscopic Study of Double Sodium-Yttrium Fluoride Crystals Doped with Erbium  $\text{Na}_{0.4}\text{Y}_{0.6}\text{F}_{2.2}:\text{Er}^{3+}$ : II. Luminescence Self-Quenching and Microparameters and Macrorates of Energy Transfer. *Optics and Spectroscopy* **2005**, *99*, 932–949.
- (23) Guyot, Y.; Collombet, A.; Somatri, T.; Tkachuk, A.; Joubert, M.-F. Spectral and Dynamic Study of the Broad Band UV  $4f^25d \rightarrow 4f^3$  Emission in Nd-Doped Double

- Sodium Yttrium Fluoride Crystals and Comparison with Nd:LiYF<sub>4</sub>. *Journal of Alloys and Compounds* **2002**, *341*, 174–178.
- (24) Huang, B.; Dong, H.; Wong, K.-L.; Sun, L.-D.; Yan, C.-H. Fundamental View of Electronic Structures of  $\beta$ -NaYF<sub>4</sub>,  $\beta$ -NaGdF<sub>4</sub>, and  $\beta$ -NaLuF<sub>4</sub>. *The Journal of Physical Chemistry C* **2016**, *120*, 18858–18870.
- (25) Ghosh, P.; Patra, A. Influence of Crystal Phase and Excitation Wavelength on Luminescence Properties of Eu<sup>3+</sup>-Doped Sodium Yttrium Fluoride Nanocrystals. *J. Phys. Chem. C* **2008**, *112*, 19283–19292.
- (26) Thoma, R. E.; Hebert, G. M.; Insley, H.; Weaver, C. F. Equilibria in the System Sodium Fluoride-Yttrium Fluoride. *Inorganic Chemistry* **1963**, *2*, 1005–1012.
- (27) Knowles, D.; Cassanho, A.; Jenssen, H. Optical Properties of Nd:NaYF<sub>4</sub> and Ho:NaYF<sub>4</sub>. *Advanced Solid State Lasers*. Washington, D.C., 1989; p CC7.
- (28) Feng, Z.; Yang, S.; Xia, H.; Wang, C.; Jiang, D.; Zhang, J.; Gu, X.; Zhang, Y.; Chen, B.; Jiang, H. Energy Transfer and 2.0  $\mu$ m Emission in Tm<sup>3+</sup>/Ho<sup>3+</sup> Co-Doped  $\alpha$ -NaYF<sub>4</sub> Single Crystals. *Materials Research Bulletin* **2016**, *76*, 279–283.
- (29) Thoma, R. E.; Insley, H.; Hebert, G. M. The Sodium Fluoride-Lanthanide Trifluoride Systems. *Inorganic Chemistry* **1966**, *5*, 1222–1229.
- (30) Wang, X.; Zhuang, J.; Peng, Q.; Li, Y.; V, T. U. Hydrothermal Synthesis of Rare-Earth Fluoride Nanocrystals. *Inorganic Chemistry* **2006**, *45*, 6661–6665.
- (31) Li, C.; Yang, J.; Quan, Z.; Yang, P.; Kong, D.; Lin, J. Different Microstructures of  $\beta$ -NaYF<sub>4</sub> Fabricated by Hydrothermal Process: Effects of pH Values and Fluoride Sources. *Chemistry of Materials* **2007**, *19*, 4933–4942.
- (32) Li, C.; Quan, Z.; Yang, P.; Huang, S.; Lian, H.; Lin, J. Shape-Controllable Synthesis and Upconversion Properties of Lutetium Fluoride (Doped with Yb<sup>3+</sup>/Er<sup>3+</sup>) Microcrystals

- by Hydrothermal Process. *The Journal of Physical Chemistry C* **2008**, *112*, 13395–13404.
- (33) Qian, L.; Zai, J.; Chen, Z.; Zhu, J.; Yuan, Y.; Qian, X. Control of the Morphology and Composition of Yttrium Fluoride via a Salt-Assisted Hydrothermal Method. *CrystEngComm* **2010**, *12*, 199–206.
- (34) Qin, X.; Wang, X.; Xiang, H.; Xie, J.; Li, J.; Zhou, Y. Mechanism for Hydrothermal Synthesis of  $\text{LiFePO}_4$  Platelets as Cathode Material for Lithium-Ion Batteries. *The Journal of Physical Chemistry C* **2010**, *114*, 16806–16812.
- (35) Yoshimura, M.; Sujaridworakun, P.; Koh, F.; Fujiwara, T.; Pongkao, D.; Ahniyaz, A. Hydrothermal Conversion of Calcite Crystals to Hydroxyapatite. *Materials Science and Engineering: C* **2004**, *24*, 521–525.
- (36) Yu, X.; Li, M.; Xie, M.; Chen, L.; Li, Y.; Wang, Q. Dopant-Controlled Synthesis of Water-Soluble Hexagonal  $\text{NaYF}_4$  Nanorods with Efficient Upconversion Fluorescence for Multicolor Bioimaging. *Nano Research* **2010**, *3*, 51–60.
- (37) Mai, H.-X.; Zhang, Y.-W.; Si, R.; Yan, Z.-G.; Sun, L.-d.; You, L.-P.; Yan, C.-H. High-Quality Sodium Rare-Earth Fluoride Nanocrystals: Controlled Synthesis and Optical Properties. *Journal of the American Chemical Society* **2006**, *128*, 6426–6436.
- (38) Fifen, J. J.; Agmon, N. Ionic Radii of Hydrated Sodium Cation from QTAIM. *The Journal of Chemical Physics* **2019**, *150*, 034304.
- (39) Nielsen, M. H.; Aloni, S.; De Yoreo, J. J. In situ TEM Imaging of  $\text{CaCO}_3$  Nucleation Reveals Coexistence of Direct and Indirect Pathways. *Science* **2014**, *345*, 1158–1162.
- (40) Grzechnik, A.; Bouvier, P.; Mezouar, M.; Mathews, M.; Tyagi, A.; Köhler, J. Hexagonal  $\text{Na}_{1.5}\text{Y}_{1.5}\text{F}_6$  at High Pressures. *Journal of Solid State Chemistry* **2002**, *165*, 159–164.

- (41) Szeftczyk, B.; Roszak, R.; Roszak, S. Structure of the Hexagonal NaYF<sub>4</sub> Phase From First-Principles Molecular Dynamics. *RSC Advances* **2014**, *4*, 22526.
- (42) Burns, J. H. Crystal Structure of Hexagonal Sodium Neodymium Fluoride and Related Compounds. *Inorganic Chemistry* **1965**, *4*, 881–886.
- (43) Palo, E.; Kankare, J.; Harju, E.; Hyppänen, I.; Hölsä, J.; Kankare, J.; Lahtinen, M.; Lastusaari, M.; Pihlgren, L.; Soukka, T. Polymorphism of NaYF<sub>4</sub>:Yb<sup>3+</sup>, Er<sup>3+</sup> Up-Conversion Luminescence Materials. *Z. Kristallogr. Proc.* 2011; pp 381–387.
- (44) Arnold, A. A.; Terskikh, V.; Li, Q. Y.; Naccache, R.; Marcotte, I.; Capobianco, J. A. Structure of NaYF<sub>4</sub> Upconverting Nanoparticles: A Multinuclear Solid-State NMR and DFT Computational Study. *The Journal of Physical Chemistry C* **2013**, *117*, 25733–25741.
- (45) Hudry, D.; Abeykoon, A. M. M.; Dooryhee, E.; Nykypanchuk, D.; Dickerson, J. H. Probing the Crystal Structure and Formation Mechanism of Lanthanide-Doped Upconverting Nanocrystals. *Chemistry of Materials* **2016**, *28*, 8752–8763.
- (46) Perera, S. S.; Amarasinghe, D. K.; Dissanayake, K. T.; Rabuffetti, F. A. Average and Local Crystal Structure of  $\beta$ -Er:Yb:NaYF<sub>4</sub> Upconverting Nanocrystals Probed by X-Ray Total Scattering. *Chemistry of Materials* **2017**, *29*, 6289–6297.
- (47) Roy, D. M.; Roy, R. Controlled Massively Defective Crystalline Solutions With the Fluorite Structure. *Journal of The Electrochemical Society* **1964**, *111*, 421.
- (48) Lee, J.; Yang, J.; Kwon, S. G.; Hyeon, T. Nonclassical Nucleation and Growth of Inorganic Nanoparticles. *Nature Reviews Materials* **2016**, *1*, 16034.
- (49) Li, D.; Soberanis, F.; Fu, J.; Hou, W.; Wu, J.; Kisailus, D. Growth Mechanism of Highly Branched Titanium Dioxide Nanowires via Oriented Attachment. *Crystal Growth & Design* **2013**, *13*, 422–428.

- (50) Yuwono, V. M.; Burrows, N. D.; Soltis, J. A.; Penn, R. L. Oriented Aggregation: Formation and Transformation of Mesocrystal Intermediates Revealed. *Journal of the American Chemical Society* **2010**, *132*, 2163–2165.
- (51) Li, D.; Nielsen, M. H.; Lee, J. R. I.; Frandsen, C.; Banfield, J. F.; De Yoreo, J. J. Direction-Specific Interactions Control Crystal Growth by Oriented Attachment. *Science* **2012**, *336*, 1014–1018.
- (52) Ivanov, V. K.; Fedorov, P. P.; Ye Baranchikov, A.; Osiko, V. V. Oriented Attachment of Particles: 100 Years of Investigations of Non-Classical Crystal Growth. *Russian Chemical Reviews* **2014**, *83*, 1204–1222.
- (53) Penn, J. M.; Banfield, A.; Perrotta, A. J.; Navrotsky, A.; Penn, R. L. Imperfect Oriented Attachment: Dislocation Generation in Defect-Free Nanocrystals. *Science (New York, N. Y.)* **1998**, *281*, 969–71.
- (54) Yin, Y.; Alivisatos, A. P. Colloidal Nanocrystal Synthesis and the Organic–Inorganic Interface. *Nature* **2005**, *437*, 664–670.
- (55) Cho, K.-S.; Talapin, D. V.; Gaschler, W.; Murray, C. B. Designing PbSe Nanowires and Nanorings through Oriented Attachment of Nanoparticles. *Journal of the American Chemical Society* **2005**, *127*, 7140–7147.
- (56) Zhang, X.; Shen, Z.; Liu, J.; Kerisit, S. N.; Bowden, M. E.; Sushko, M. L.; De Yoreo, J. J.; Rosso, K. M. Direction-Specific Interaction Forces Underlying Zinc Oxide Crystal Growth by Oriented Attachment. *Nature Communications* **2017**, *8*, 835.
- (57) Frandsen, C.; Legg, B. A.; Comolli, L. R.; Zhang, H.; Gilbert, B.; Johnson, E.; Banfield, J. F. Aggregation-Induced Growth and Transformation of  $\beta$ -FeOOH Nanorods to Micron-Sized  $\alpha$ -Fe<sub>2</sub>O<sub>3</sub> Spindles. *CrystEngComm* **2014**, *16*, 1451–1458.

- (58) Nielsen, M. H.; Li, D.; Zhang, H.; Aloni, S.; Han, T. Y.-J.; Frandsen, C.; Seto, J.; Banfield, J. F.; Cölfen, H.; De Yoreo, J. J. Investigating Processes of Nanocrystal Formation and Transformation via Liquid Cell TEM. *Microscopy and Microanalysis* **2014**, *20*, 425–436.
- (59) Sanders, T. MATLAB Imaging Algorithms: Image Reconstruction, Restoration, and Alignment, With a Focus in Tomography. <http://www.toby-sanders.com/software>, <https://doi.org/10.13140/RG.2.2.33492.60801>, <https://doi.org/10.13140/RG.2.2.33492.60801>.
- (60) Suloway, C.; Pulokas, J.; Fellmann, D.; Cheng, A.; Guerra, F.; Quispe, J.; Stagg, S.; Potter, C. S.; Carragher, B. Automated Molecular Microscopy: The New Legion System. *Journal of Structural Biology* **2005**, *151*, 41–60.
- (61) Newville, M. IFEFFIT: Interactive XAFS Analysis and FEFF Fitting. *Journal of Synchrotron Radiation* **2001**, *8*, 322–324.
- (62) Ravel, B.; Newville, M. ATHENA, ARTEMIS, HEPHAESTUS: Data Analysis for X-ray Absorption Spectroscopy Using IFEFFIT. *Journal of Synchrotron Radiation* **2005**, *12*, 537–541.
- (63) Manceau, A.; Combes, J. M. Structure of Mn and Fe Oxides and Oxyhydroxides: A Topological Approach by EXAFS. *Physics and Chemistry of Minerals* **1988**, *15*, 283–295.
- (64) Michalowicz, A.; Girerd, J. J.; Goulon, J. EXAFS Determination of the Copper Oxalate Structure. Relation Between Structure and Magnetic Properties. *Inorganic Chemistry* **1979**, *18*, 3004–3010.
- (65) Ghosh, P.; Kar, A.; Patra, A. Energy Transfer Study Between Ce<sup>3+</sup> and Tb<sup>3+</sup> Ions in Doped and Core-Shell Sodium Yttrium Fluoride Nanocrystals. *Nanoscale* **2010**, *2*, 1196.

- (66) Tkachuk, A. M.; Ivanova, S. É.; Joubert, M. F.; Guyot, Y. Spectroscopic Study of Double Sodium-Yttrium Fluoride Crystals Doped with Erbium  $\text{Na}_{0.4}\text{Y}_{0.6}\text{F}_{2.2}:\text{Er}^{3+}$ : I. Intensities of Luminescence Spectra and Kinetics of Luminescence. *Optics and Spectroscopy* **2004**, *97*, 251–269.
- (67) Auzel, F.; Goldner, P. Towards Rare-Earth Clustering Control in Doped Glasses. *Optical Materials* **2001**, *16*, 93–103.
- (68) Gao, G.; Wei, J.; Shen, Y.; Peng, M.; Wondraczek, L. Heavily  $\text{Eu}_2\text{O}_3$ -Doped Yttria-Aluminoborate Glasses for Red Photoconversion With a High Quantum Yield: Luminescence Quenching and Statistics of Cluster Formation. *J. Mater. Chem. C* **2014**, *2*, 8678–8682.
- (69) Johnson, N. J. J.; He, S.; Diao, S.; Chan, E. M.; Dai, H.; Almutairi, A. Direct Evidence for Coupled Surface and Concentration Quenching Dynamics in Lanthanide-Doped Nanocrystals. *Journal of the American Chemical Society* **2017**, *139*, 3275–3282.
- (70) Scherrer, P. Bestimmung der Größe und der inneren Struktur von Kolloidteilchen mittels Röntgenstrahlen. *Nachrichten von der Gesellschaft der Wissenschaften zu Göttingen, Mathematisch-Physikalische Klasse* **1918**, *2*, 98–100.
- (71) Cullity, B. D. *Elements of X-Ray Diffraction, Second Edition*; 1978; pp 99–106.
- (72) Dove, P. M.; Han, N.; De Yoreo, J. J. Mechanisms of Classical Crystal Growth Theory Explain Quartz and Silicate Dissolution Behavior. *Proceedings of the National Academy of Sciences* **2005**, *102*, 15357–15362.
- (73) De Yoreo, J. J.; Zepeda-Ruiz, L. A.; Friddle, R. W.; Qiu, S. R.; Wasylenki, L. E.; Chernov, A. A.; Gilmer, G. H.; Dove, P. M. Rethinking Classical Crystal Growth Models Through Molecular Scale Insights: Consequences of Kink-Limited Kinetics. *Crystal Growth & Design* **2009**, *9*, 5135–5144.

- (74) Erdemir, D.; Lee, A. Y.; Myerson, A. S. Nucleation of Crystals From Solution: Classical and Two-Step Models. *Accounts of Chemical Research* **2009**, *42*, 621–629.
- (75) Williams, D. B.; Carter, C. B. *Transmission Electron Microscopy: A Textbook for Materials Science*; 2009; pp 389–405.
- (76) Williams, D. B.; Carter, C. B. *Transmission Electron Microscopy: A Textbook for Materials Science*; 2009; pp 211–219.
- (77) Zhang, H.; De Yoreo, J. J.; Banfield, J. F. A Unified Description of Attachment-Based Crystal Growth. *ACS Nano* **2014**, *8*, 6526–6530.
- (78) Sui, Y.; Tao, K.; Tian, Q.; Sun, K. Interaction Between  $Y^{3+}$  and Oleate Ions for the Cubic-to-Hexagonal Phase Transformation of  $NaYF_4$  Nanocrystals. *The Journal of Physical Chemistry C* **2012**, *116*, 1732–1739.
- (79) Reimer, L.; Rennekamp, R. Imaging and Recording of Multiple Scattering Effects by Angular-Resolved Electron Energy-Loss Spectroscopy. *Ultramicroscopy* **1989**, *28*, 258–265.
- (80) Nakouzi, E.; Soltis, J. A.; Legg, B. A.; Schenter, G. K.; Zhang, X.; Graham, T. R.; Rosso, K. M.; Anovitz, L. M.; De Yoreo, J. J.; Chun, J. Impact of Solution Chemistry and Particle Anisotropy on the Collective Dynamics of Oriented Aggregation. *ACS Nano* **2018**, *12*, 10114–10122.
- (81) Kanhere, P. D.; Zheng, J.; Chen, Z. Site Specific Optical and Photocatalytic Properties of Bi-Doped  $NaTaO_3$ . *The Journal of Physical Chemistry C* **2011**, *115*, 11846–11853.

# Graphical TOC Entry

